

# An $r$ - $h$ Adaptive Kinematic Approach for 3D Limit Analysis

Zhenhao Shi<sup>a</sup>, James P. Hambleton<sup>a,b,\*</sup>

<sup>a</sup>*Department of Civil and Environmental Engineering, Northwestern University,  
Evanston, IL 60208, USA*

<sup>b</sup>*School of Engineering, University of Newcastle, Callaghan, NSW 2308, Australia*

---

## Abstract

This paper explores a pathway for increasing efficiency in numerical 3D limit analysis through  $r$ - $h$  adaptivity, wherein nodal positions ( $r$ ) and element lengths ( $h$ ) are successively refined. The approach uses an iterative, nested optimization procedure involving three components: (1) determination of velocities for a fixed mesh of rigid, translational elements (blocks) using second-order cone programming; (2) adaptation of nodal positions using non-linear optimization ( $r$  adaptivity); and (3) subdivision of elements based on the magnitude of the velocity jumps ( $h$  adaptivity). Examples show that the method can compute reasonably accurate limit loads at relatively low computational cost.

*Keywords:* limit analysis, 3D, kinematic method, upper bound, adaptivity

---

\*Corresponding author. Address: Department of Civil and Environmental Engineering, Northwestern University, Technological Institute A122, 2145 Sheridan Road, Evanston, IL 60208; Tel.: +1 847 491 4858

Email addresses: [zhenhao.shi@northwestern.edu](mailto:zhenhao.shi@northwestern.edu) (Zhenhao Shi), [jphambleton@northwestern.edu](mailto:jphambleton@northwestern.edu) (James P. Hambleton)

**1 1. Introduction**

2 Accurate evaluation of the limit load, or collapse load, causing failure of  
3 a mass of geomaterial is crucial for the design of geotechnical infrastructure,  
4 including foundations, slopes, and earth retaining systems. Limit load com-  
5 putations are also central in the determination of how to induce failure de-  
6 liberately, as in excavation, mining, and earthmoving (e.g., Hettiaratchi and  
7 Reece, 1974; Godwin and O'Dogherty, 2007; Hambleton et al., 2014; Ham-  
8 bleton, 2017). Many models rely on a two-dimensional (2D) idealization of  
9 the true configuration (e.g., plane strain or axisymmetry), which significantly  
10 simplifies the calculations. However, in many cases, the three-dimensional  
11 (3D) nature of the problem cannot be ignored. When 3D conditions pre-  
12 vail, computations based on the 2D simplification can overestimate or un-  
13 derestimate the limit load (Soubra and Regenass, 2000; Antão et al., 2011;  
14 Michalowski, 2001; Griffiths and Marquez, 2007; Michalowski and Drescher,  
15 2009; Wördem and Achmus, 2013).

16 Among various existing methods, the kinematic approach of limit anal-  
17 ysis is a particularly effective and useful means of evaluating limit loads  
18 (cf. Chen, 1975). The kinematic theorem states that for any kinematically  
19 admissible velocity field (i.e., failure or collapse mechanism), the load com-  
20 puted by equating the work rate of external forces to the internal energy  
21 dissipation rate is a rigorous bound on the true limit load. It gives an upper  
22 bound for a load inducing collapse and a lower bound for a load resisting  
23 collapse (Drescher, 1991). A kinematically admissible velocity field is one  
24 that satisfies boundary conditions and the plastic flow rule. The kinematic  
25 theorem requires that material is perfectly plastic and obeys the associative

26 flow rule. The consequences of associativity and possible workarounds in  
27 instances where it may lead to unrealistic predictions are discussed by vari-  
28 ous authors (Davis, 1968; Davis and Booker, 1971; Chen, 1975; Drescher and  
29 Detournay, 1993; Krabbenhoft et al., 2012; Sloan, 2013). For 3D problems  
30 with simple geometries and loading conditions, a kinematically admissible  
31 mechanism can be constructed manually, thereby permitting an analytical  
32 or semi-analytical solution (e.g., Murray and Geddes 1987; Soubra and Re-  
33 genass 2000; Michalowski 2001). Nevertheless, it is generally difficult to  
34 construct collapse mechanisms for 3D problems, and numerical methods are  
35 usually necessary.

36 Finite element limit analysis (FELA) is a powerful numerical implemen-  
37 tation that can evaluate 3D collapse loads without assuming a failure mech-  
38 anism *a priori* (Lyamin and Sloan, 2002a,b; Lyamin et al., 2007; Vicente da  
39 Silva and Antão, 2008; Krabbenhøft et al., 2008; Martin and Makrodimopou-  
40 los, 2008; Sloan, 2013). As in the conventional finite element method (FEM),  
41 FELA discretizes the domain into elements and interpolates the velocity field  
42 based on discrete values at nodes and the assumed shape functions. The opti-  
43 mal velocity field is computed by solving a large-scale optimization problem.  
44 The objective function corresponds to the limit load, and the unknown nodal  
45 velocities are constrained by enforcing kinematically admissibility. In FELA,  
46 a certain discretization of the domain (i.e., meshing) leads only to a subset  
47 of all possible velocity fields. Therefore, the limit load computed by FELA  
48 is often highly sensitive to the finite element mesh, particularly in regions of  
49 localized deformation. To maximize the solution accuracy using a minimum  
50 number of elements, adaptive mesh refinement techniques (i.e.,  $h$  adaptivity)

51 have been proposed to automatically refine regions featuring large gradients  
52 (Borges et al., 1999, 2001; Lyamin et al., 2005; Martin, 2011) or large gaps be-  
53 tween upper-bound and lower-bound solutions computed on the same mesh  
54 (Ciria et al., 2008; Muñoz et al., 2009). The concept of  $h$  adaptivity has  
55 played a key role in improving the accuracy and computational efficiency of  
56 2D analyses. In contrast, 3D FELA based on adaptive mesh refinement (e.g.,  
57 Dunne and Martin, 2017) and its performance have not been investigated in  
58 great detail.

59 Another general numerical approach referred to as discontinuity layout  
60 optimization (DLO) has been developed by Smith and Gilbert (2007) and  
61 Hawksbee et al. (2013) on the basis of optimizing a velocity field consisting  
62 only of so-called velocity discontinuities, which represent infinitesimally thin  
63 zones of shearing. DLO focuses on optimizing the arrangement of these  
64 discontinuities, with the tacit assumption that the material enclosed by the  
65 discontinuities is rigid. This method searches for an optimal combination of  
66 the possible discontinuities interconnecting a *fixed* grid of nodes. Because the  
67 grid is fixed, the grid resolution has to be refined to capture intricate features  
68 or reasonably represent a continuous velocity field, which can dramatically  
69 increase the number of potential discontinuities at the cost of computational  
70 expediency (Hawksbee et al., 2013).

71 While the above-mentioned numerical approaches represent valuable tools  
72 to evaluate limit loads for 3D problems, they tend to be computationally in-  
73 tensive. In many cases, the optimal mechanism is in fact relatively simple,  
74 and the standard formulations of FELA and DLO can be unnecessarily oner-  
75 ous. Furthermore, the computational demands of existing techniques impose

76 a significant limitation for the emerging computational approach referred to  
77 in this paper as the sequential kinematic method (SKM). In SKM, kinematic  
78 solutions are sequentially computed as a means of simulating a full process of  
79 deformation, and the optimal velocity field within any particular increment  
80 is used to update the model geometry and material properties. Given its  
81 computational efficiency and stability, SKM has become a compelling alter-  
82 native to conventional techniques such as FEM for simulating problems in  
83 which capturing the evolution of material boundaries is critical (Hambleton  
84 and Drescher, 2012; Mary et al., 2013; Hambleton et al., 2014; Kong et al.,  
85 2017). In particular, SKM shows a remarkable capability in modeling the  
86 large deformation of cohesionless soils (Hambleton et al., 2014; Kashizadeh  
87 et al., 2014), which poses a significant challenge for conventional approaches.  
88 Current SKM formulations, however, are restricted to 2D. Extension to 3D  
89 has been largely halted by the lack of efficient methods to compute the op-  
90 timal velocity field within each increment of simulation.

91 In this work, we investigate the concept of  $r$  adaptivity, in combination  
92 with  $h$  adaptivity, and assess the potential of this approach for increasing  
93 computational efficiency in 3D limit analysis. Pioneered in the earlier work  
94 of Johnson (1995) and more recently explored for 2D limit analysis (Mi-  
95 lani and Lourenço, 2009; Hambleton and Sloan, 2013; Milani, 2015; He and  
96 Gilbert, 2016; Muñoz et al., 2018),  $r$  adaptivity improves the computed limit  
97 load by explicitly optimizing the *nodal positions* that control the locations  
98 of possible velocity discontinuities. Because relatively coarse meshes with  
99 suitably placed edges (velocity discontinuities) are often sufficient to obtain  
100 accurate solutions, kinematic FELA and DLO enriched with  $r$  adaptivity of-

101 fers a promising pathway for improving efficiency, as previously demonstrated  
102 for 2D formulations.

103 **2. Overview of the  $r$ - $h$  adaptive approach**

104 The general concept we explore in this paper is to start with a simple ve-  
105 locity field, one requiring minimal computational effort, and then refine this  
106 field to improve the accuracy of the computed limit load and collapse mech-  
107 anism. We adopt a formulation in which the velocity field is characterized  
108 by discrete regions (blocks or elements) of translational motion separated by  
109 velocity discontinuities. These elements are tetrahedral by assumption, such  
110 that the edges, representing velocities discontinuities, are planar. We restrict  
111 our attention to material obeying the Mohr-Coulomb yield criterion and as-  
112 sume that the internal friction angle  $\phi$  and cohesion  $c$  are constant across  
113 the soil mass. Similarly, the material unit weight, denoted by  $\gamma$ , is assumed  
114 to be constant. Spatially varied  $\phi$ ,  $c$ , and  $\gamma$  can be included into the current  
115 formulation by constructing mesh according to the soil stratigraphy, in that  
116 no discontinuity spans across different layers of soils. In the case of inter-  
117 layer discontinuities, the highest angle of friction and cohesion encountered  
118 should be used to maintain the upper-bound status of the solution.

119 Starting from an initial arrangement (mesh) of elements, the proposed  
120  $r$ - $h$  adaptive approach proceeds iteratively, and each iteration involves three  
121 key components. First, as explained in detail in Section 3, the optimal ve-  
122 locities for a fixed mesh are determined using second-order cone program-  
123 ming (SOCP). Second, as described in Section 4, the nodal positions are  
124 regarded as variables determined through non-linear optimization ( $r$  adap-

125 tivity). Third, elements are potentially subdivided ( $h$  adaptivity). Section  
 126 5 and 6 explain this third step and how each of the three components are  
 127 combined to obtain a complete solution algorithm, respectively. Section 7  
 128 considers several example problems to which the algorithm is applied.

129 **3. Optimization of the velocity field for a fixed mesh**

130 Considering an arbitrary mesh of rigid tetrahedral elements (blocks),  
 131 Hambleton and Sloan (2016) proposed a technique that utilizes second-order  
 132 cone programming (SOCP) to search for a kinematically admissible velocity  
 133 field that yields an optimal limit load and collapse mechanism. For com-  
 134 pleteness, its mathematical formulation is summarized here.

135 A generic pair of blocks is depicted in Fig. 1(a). The velocity jump  
 136 between these blocks is denoted by  $\Delta v_i$  and is calculated as  $\Delta v_i = v_i^I - v_i^{II}$ ,  
 137 where  $v_i^I$  and  $v_i^{II}$  are the block velocities. The superscripts  $I$  and  $II$  indicate,  
 138 arbitrarily, the first and second block, and the index  $i = 1, 2, 3$  indicates the

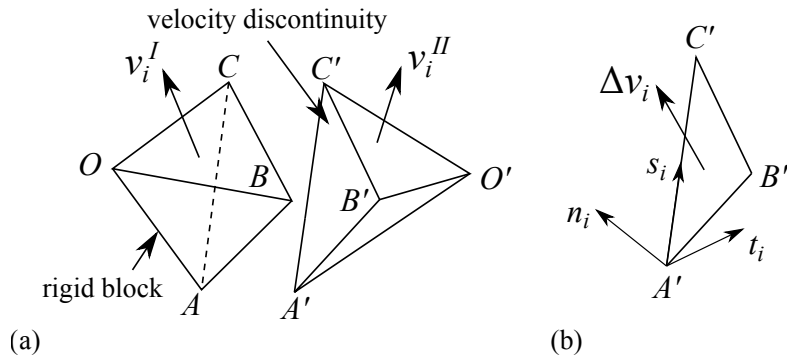


Figure 1: Schematics showing (a) 3D rigid blocks separated by a planar velocity discontinuity and (b) the definition of a local coordinate system associated with the discontinuity plane.

139 velocity component. In this work, the component associated with  $i = 3$  is  
 140 always in the vertical direction, and it is assumed to be positive when the  
 141 velocity is upward (i.e., opposite the direction of gravity). Chen (1975) shows  
 142 that for materials obeying the Mohr-Coulomb yield criterion, the energy  
 143 dissipation rate along the planar velocity discontinuities between elements  
 144 (blocks) can be expressed as

$$\dot{d} = cA|\Delta v_t| \quad (1)$$

145 The variable  $A$  denotes the area, and  $\Delta v_t$  is the tangential velocity jump with  
 146 respect to the plane of the discontinuity. The absolute value is prescribed  
 147 so that the dissipated power is always positive, regardless of the shearing  
 148 direction. To fulfill the associative flow rule corresponding to the Mohr-  
 149 Coulomb yield condition, a kinematically admissible velocity discontinuity  
 150 has to meet the following “jump condition” (Chen, 1975):

$$\Delta v_n = |\Delta v_t| \tan \phi \quad (2)$$

151 The variable  $\Delta v_n$  denotes the normal velocity jump. By adopting the local  
 152 coordinate system shown in Fig. 1(b), Eqs. (1) and (2) can be rewritten as

$$\begin{aligned} \dot{d} &= cA\sqrt{(\Delta v_i t_i)^2 + (\Delta v_i s_i)^2} \\ \Delta v_i n_i &= \tan \phi \sqrt{(\Delta v_i t_i)^2 + (\Delta v_i s_i)^2} \end{aligned} \quad (3)$$

153 Following the summation convention, the quantities  $\Delta v_i t_i$  and  $\Delta v_i s_i$  are dot  
 154 products calculated, for example, as  $\Delta v_i t_i = \Delta v_1 t_1 + \Delta v_2 t_2 + \Delta v_3 t_3$ . In  
 155 Eq. (3),  $n_i$  is a unit vector normal to the plane of the discontinuity, and  $t_i$   
 156 and  $s_i$  are two unit vectors parallel to the plane. These three vectors give a  
 157 mutually orthogonal transformed basis for expressing the velocity vectors, as

depicted in Fig. 1(b). Note that in accordance with measuring the velocity jump from block  $I$  to  $II$  discussed above, the vector  $n_i$  points towards block  $I$  such that a positive normal component of the velocity jump indicates dilation.

In order to write Eq. (3) in a form amenable to SOCP, the quantity  $\sqrt{(\Delta v_i t_i)^2 + (\Delta v_i s_i)^2}$  is replaced by a dummy variable  $\mu$ :

$$\begin{aligned}\dot{d} &= cA\mu \\ \Delta v_i n_i &= \mu \tan \phi\end{aligned}\tag{4}$$

The dummy variable  $\mu$  is then constrained as follows:

$$\mu \geq \sqrt{(\Delta v_i t_i)^2 + (\Delta v_i s_i)^2}\tag{5}$$

Eq. (5) is in the form of a so-called second-order cone constraint, one of the types permitted in SOCP in addition to linear equality and inequality constraints (cf. Sturm, 2002).

We note that the expressions given by Eq. (4) are exact only in the particular instance where strict equality is achieved in Eq. (5):

$$\mu = \sqrt{(\Delta v_i t_i)^2 + (\Delta v_i s_i)^2}\tag{6}$$

Equality is achieved by constructing the optimization problem such that the dummy variable  $\mu$  is minimized, and thus  $\mu$  is driven to equality as in Eq. (6). Application to example problems, such as those considered in Section 7.3, reveals that equality is achieved in most cases. However, in the case of cohesionless material ( $c = 0$ ) for which the dissipation  $\dot{d}$  vanishes, equality is not always achieved. Nevertheless, it should be noted that, when the equality in Eq. (5) is not satisfied, the solution remains an upper bound of the true collapse load because the energy dissipation and the jump condition

177 are effectively computed according to a larger cohesion and friction angle,  
 178 respectively.

179 By equating the rate of internal energy dissipation to the work rate of  
 180 external forces for an assembly of elements (blocks), one obtains

$$\sum_{j=1}^{N_D} \dot{d}_j = - \sum_{k=1}^{N_B} \gamma V_k v_{3k} + \int_{S^*} t_i^* v_i ds + \int_S t_i v_i ds \quad (7)$$

181 In Eq. (7),  $N_D$  and  $N_B$  are the number of discontinuity planes and the number  
 182 of blocks, respectively, and subscripts  $j$  and  $k$  are used to indicate quantities  
 183 corresponding to the  $j^{\text{th}}$  discontinuity plane and the  $k^{\text{th}}$  block. The variable  
 184  $V_k$  denotes the volume of the  $k^{\text{th}}$  block, a readily computed constant for a  
 185 fixed mesh. The three terms on the right side of Eq. (7) represent the work  
 186 rate of body forces, fixed surface tractions ( $t_i^*$ ) and tractions along the surface  
 187 where the limit loads is evaluated ( $t_i$ ), respectively.

188 Drescher (1991), Sloan (1995), and Michalowski (2001) among others  
 189 show how Eq. (7) can be manipulated to obtain various expressions of the  
 190 limit load. A case encompassing all examples considered in Section 7 is  
 191 that the direction of  $t_i$  is fixed, or known *a priori*, and velocities along the  
 192 boundary  $S$  are uniform, as could occur for a rigid footing or translational  
 193 retaining wall. In this instance, the unknown traction  $t_i$  is expressed in  
 194 terms of a fixed traction  $t_i^*$  as  $t_i = \lambda t_i^*$ , where  $\lambda \geq 0$  is an unknown multi-  
 195 plier dictating the magnitude of the limit load. The last term in Eq. (7) is  
 196  $\int_S t_i v_i ds = v_i \int_S \lambda t_i^* ds = \lambda v_i F_i^*$ , where  $F_i^* = \int_S t_i^* ds$  is the resultant force.  
 197 The magnitude of the velocity is arbitrary (cf. Chen, 1975), and thus one  
 198 can write  $v_i F_i^* = \alpha$ , where  $\alpha$  is an arbitrary constant. Equation (7) can then

<sup>199</sup> be manipulated to write:

$$\lambda = \frac{1}{\alpha} \left( \sum_{j=1}^{N_D} \dot{d}_j + \sum_{k=1}^{N_B} \gamma V_k v_{3k} - \int_{S^*} t_i^* v_i ds \right) \quad (8)$$

<sup>200</sup> Here we assume  $\alpha$  is unity (a value of 1 with appropriate units) for convenience. Depending on the distribution of the fixed tractions  $t_i^*$ , the final term <sup>201</sup> in parenthesis in Eq. (7) can be integrated to obtain a sum over the unknown <sup>202</sup> velocities, viz. <sup>203</sup>

$$\int_{S^*} t_i^* v_i ds = \sum_{l=1}^{N_F} \beta_{il} v_{il} \quad (9)$$

<sup>204</sup> In Eq. (9),  $N_F$  is the number of elements with fixed tractions, and  $\beta_{il}$  ( $i = 1, 2, 3; l = 1, \dots, N_F$ ) are constant coefficients. The notation  $v_{il}$  again indicates <sup>205</sup> the  $i^{\text{th}}$  velocity component of the  $l^{\text{th}}$  element. <sup>206</sup>

<sup>207</sup> Finally, the optimization of the velocity field for a fixed mesh is written <sup>208</sup> in the standard form of SOCP as follows:

$$\begin{aligned} \min \quad & \lambda = \sum_{j=1}^{N_D} \dot{d}_j + \sum_{k=1}^{N_B} \gamma V_k v_{3k} - \sum_{l=1}^{N_F} \beta_{il} v_{il} \\ \text{s.t.} \quad & \Delta v_{ij} n_{ij} = \mu_j \tan \phi \quad j = 1, \dots, N_D \\ & \dot{d}_j = c A_j \mu_j \quad j = 1, \dots, N_D \\ & \mu_j \geq \sqrt{(\Delta v_{ij} t_{ij})^2 + (\Delta v_{ij} s_{ij})^2} \quad j = 1, \dots, N_D \end{aligned} \quad (10)$$

<sup>209</sup> For a load resisting collapse, where the work rate of the unknown tractions <sup>210</sup> on the velocity is negative, the kinematic theorem of limit analysis leads to <sup>211</sup> a lower bound on the true collapse load (cf. Drescher, 1991). To compute <sup>212</sup> such a lower bound, Eq. (10) is converted to a maximization problem by <sup>213</sup> minimizing the negative of the objective function. In this work, the Mosek

214 toolbox integrated with MATLAB (Mosek, 2015) is employed to solve the  
 215 SOCP problem.

216 Upon solving the SOCP problem of Eq. (10), one obtains an optimal  
 217 value for the load multiplier, denoted by  $\lambda_{opt}$ . The computed bound on the  
 218 true collapse load is then simply

$$F_i = \lambda_{opt} F_i^* \quad (11)$$

219 **4. Optimization of nodal positions ( $r$  adaptivity)**

220 The bound on the limit load computed using Eq. (10) depends strongly  
 221 on the positions of the nodes within the mesh that define the locations of  
 222 potential velocity discontinuities. In particular, the optimal velocity field  
 223 and load multiplier  $\lambda_{opt}$  depend on the coordinates of the nodes that are not  
 224 constrained by boundary conditions or symmetry, and are therefore free to  
 225 move. The coordinates of these nodes are denoted by  $x_{im}$ . Index  $i$  again  
 226 gives the component ( $i = 1, 2, 3$ ), and index  $m$  ( $i = 1, \dots, N_R$ ) identifies each  
 227 of the free nodes.

228 For the purpose of optimizing the nodal positions, a non-linear optimiza-  
 229 tion problem is formulated as follows:

$$\begin{aligned} \min \quad & \lambda_{opt}(x_{im}) \\ \text{s.t.} \quad & V_k(x_{im}) \geq 0 \quad k = 1, \dots, N_B \\ & x_{im}^l \leq x_{im} \leq x_{im}^u \end{aligned} \quad (12)$$

230 This non-linear optimization is nested with the SOCP described above, in  
 231 that the objective function in Eq. (12) is the load multiplier computed for  
 232 a given set of nodal positions  $x_{im}$  ( $i = 1, 2, 3$ ;  $m = 1, \dots, N_R$ ), defined and

evaluated in precisely the same way as in Section 3. To prevent the interpenetration of elements and ensure computational stability, the first set of constraints in Eq. (12) requires that element volume  $V_k$  ( $k = 1, \dots, N_B$ ) is always positive. It should be noted that we permit the possibility  $V_k = 0$ , thus allowing elements to collapse to transition layers with zero thickness. The variables  $x_{im}^l$  and  $x_{im}^u$  appearing in the second set of inequality constraints define allowable limits for certain nodal position components. For instance, the  $z$ -coordinate of the ground surface is an upper bound on the position of all nodes along the  $z$ -direction.

Due to boundary conditions and symmetry, some of the position components ( $x$ ,  $y$ , and  $z$ ) are fixed. Rather than imposing constraints, the total number of free variables introduced in the non-linear optimization problem of Eq. (12) is condensed from  $3N_R$  to  $DOF$ , where  $DOF = 3N_R - N_{FC}$  and  $N_{FC}$  is the total number of fixed position components.

As the objective function and constraints are non-linear functions of the free (unknown) variables  $x_{im}$ , the optimization problem of Eq. (12) falls within the general domain of non-linear constrained optimization. A preliminary study employs two algorithms embedded in the FMINCON solver of MATLAB to solve this problem: the interior point method (IPM) and sequential quadratic programming (SQP). Both methods represent the state of the art in solving general constrained optimization problems. It is found that these two methods can achieve similar solutions. However, IPM requires more iterations, and during some iteration processes it diverges (i.e., the objective function increases rather than decreases). Accordingly, SQP is used throughout this work. It should be noted that the theoretical reason why

258 SQP outperforms IPM remains unclear. This is due in part to the lack of an  
259 explicit expression for the objective function in the constrained optimization  
260 problem (i.e., the objective function itself is the SOCP problem defined in  
261 Eq. (10)).

262 To determine when to stop the iterations for solving the optimization  
263 problem of Eq. (12), we adopt two criteria, and the satisfaction of either  
264 one is assumed to signal the convergence to a solution. Specifically, the  
265 optimization ends once (1) the quantity referred to as “first-order optimality”  
266 is lower than a tolerance,  $\text{opt}_{tol}$ , or (2) the norm of the vector containing the  
267 changes of nodal positions during an iteration is lower than a tolerance,  
268  $\Delta x_{tol}$ . First-order optimality, described in greater detail by Nocedal and  
269 Wright (2006), is a well-known and widely used measure of how close the  
270 current solution is to optimal. We use the second criterion to cease iterations  
271 when  $r$  adaptivity produces only minor perturbations that lead to marginal  
272 improvement the computed limit load. The following tolerance values are  
273 employed in this work:  $\text{opt}_{tol} = 1E^{-2}$  and  $\Delta x_{tol} = 1E^{-2}$ . The usage of  
274 lower tolerances increases the number of iterations but does not noticeably  
275 improve the solution. For detailed descriptions of the above stopping criteria  
276 and their implementation in MATLAB, the reader is referred to Nocedal and  
277 Wright (2006) and The MathWorks, Inc (2018).

278 **5. Element subdivision ( $h$  adaptivity)**

279 Once  $r$  adaptivity is applied to optimize the limit load and velocity field  
280 for a particular mesh topology (element number and connectivity), further  
281 improvement of the solution requires either uniformly or selectively refining

282 the mesh. This section proposes a strategy to refine the mesh by selectively  
283 dividing elements, such that refinement will only be performed as needed and  
284 at locations that potentially improve the solution.

285 Any subdivision strategy must decide where to refine the mesh based  
286 on certain *a posteriori* indicators (i.e., information derived from the current  
287 computation). For a rigid block system, a simple indicator is the magni-  
288 tude of the velocity jump, which is proportional to the integral of strain rate  
289 over the infinitesimally thin layers between adjacent elements (Chen, 1975)  
290 represented as velocity discontinuities. The magnitude of the velocity jump  
291 therefore identifies regions characterized by high strain rate, and mesh re-  
292 finement in these regions typically has the highest potential for improving  
293 the solution. This concept is similar to the adaptive mesh refinement pro-  
294 posed by Martin (2011) for FELA, which attempts to evenly distribute the  
295 integral of the maximum shear strain rate over all elements, such that the  
296 concentration of elements reflects the intensity of the shearing rate (change  
297 of velocity). The specific subdivision criterion postulated in this work is to  
298 subdivide elements sharing an edge for which the magnitude of the velocity  
299 jump is greater than a tolerance  $\Delta v_{tol}$ , i.e.,  $\sqrt{\Delta v_i \Delta v_i} \geq \Delta v_{tol}$ .

300 The flow chart within the dashed box of Fig. 2 presents the basic algo-  
301 rithm iterated over all elements to perform the subdivision. This algorithm  
302 first filters out elements with nearly zero velocity or small volume through  
303 prescribed tolerances  $v_{tol}$  and  $V_{tol}$ , respectively. The former filtering prevents  
304 unnecessary refinement in stationary regions, and the latter contributes to  
305 forming the best overall shape of the mechanism, excluding the partition of  
306 small elements that tend only to result in small and localized improvement

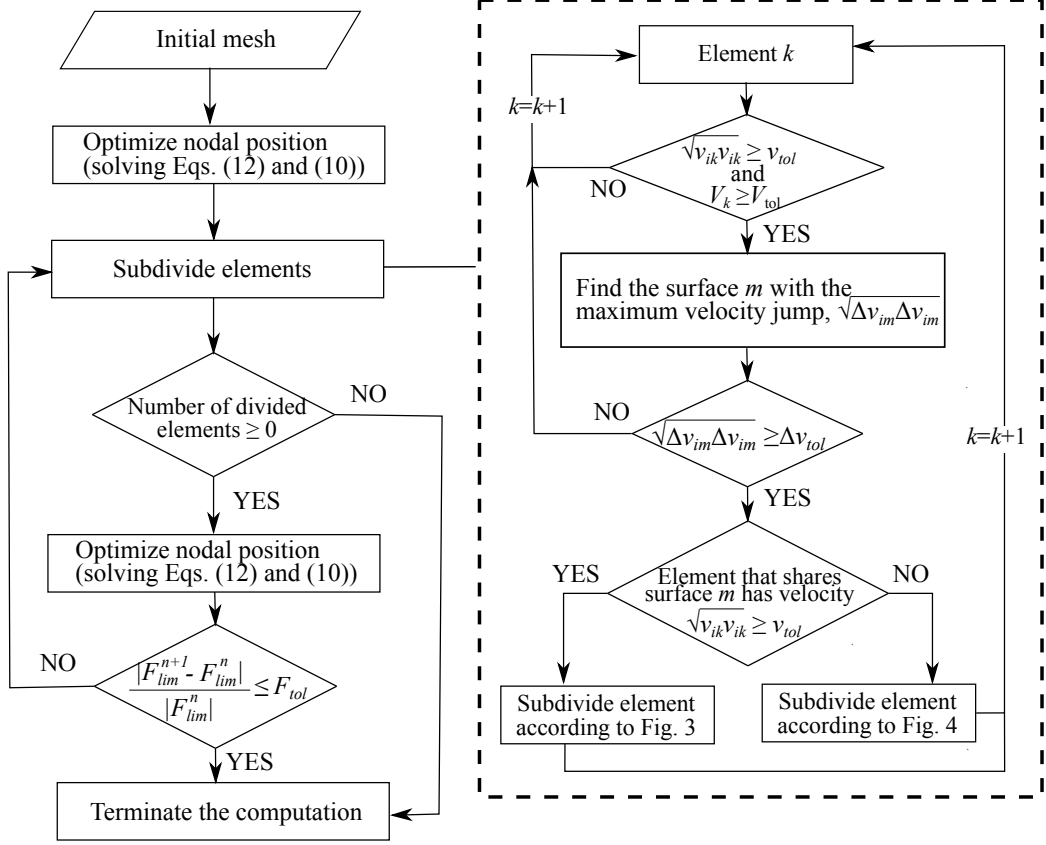


Figure 2: Computation flow chart of the proposed  $r$ - $h$  adaptive approach.

307 of the collapse mechanism. Each element that passes this first screening and  
 308 has edges with  $\sqrt{\Delta v_i \Delta v_i} \geq \Delta v_{tol}$  will be subdivided according to either Fig. 3  
 309 or Fig. 4, depending on whether this velocity jump is between two moving  
 310 elements (i.e., both have velocity greater than  $v_{tol}$ ), or between a moving  
 311 element and a stationary region.

312 As depicted in Fig. 3, when the targeted velocity jump is between two  
 313 moving elements, we propose two different approaches to subdivide the el-  
 314 ement corresponding to the subfigures (a) and (b). The adoption of one

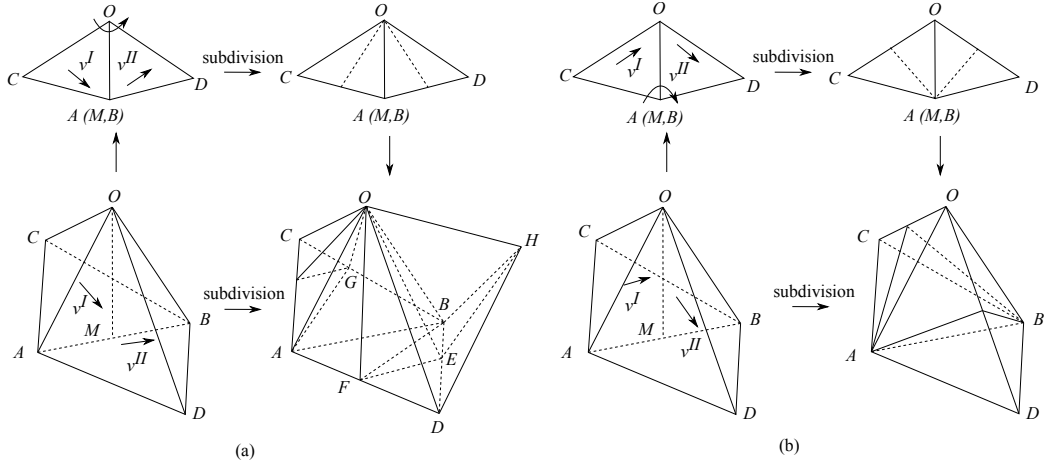


Figure 3: Schematic showing the subdivision of a pair of blocks based on the flow direction of the local velocity field.

315 of these two alternatives depends on *the flow direction of the local velocity*  
 316 *field*. Fig. 3 shows the two possibilities: a flow tending to “rotate” about the  
 317 point  $O$ , as shown in subfigure (a), or rotate about the axis  $AB$ , as shown in  
 318 subfigure (b). Identifying this flow direction is important because regional  
 319 velocity jumps can be reduced (smoothed) when more elements are added  
 320 aligning with this direction.

321 For the scenario shown in Fig. 3(a), the blocks  $OABC$  and  $OADB$  are  
 322 divided so that the newly added discontinuities radiate from the point  $O$   
 323 and bisect the edges  $AC$ ,  $BC$ ,  $AD$  and  $BD$ . Note that for illustration pur-  
 324 poses, we have assumed the surface  $OAB$  possesses the maximum velocity  
 325 jump for both blocks; otherwise, only one block is subdivided. Fig. 3(a) also  
 326 shows that the subdivision of the targeted element  $OADB$  adds a new node  
 327  $E$  to the edge  $BD$ , which is shared by an adjacent element  $ODBH$ . These  
 328 neighboring elements will automatically be partitioned by new discontinuities

329 passing through the new nodes (e.g., the new discontinuity  $OEH$  is created  
 330 to pass through the node  $E$  in Fig. 3(a)). Without such partition of neigh-  
 331 boring elements, subsequently changing the positions of the new nodes (e.g.,  
 332 the node  $E$ ) can lead to interpenetration or gaps between the newly formed  
 333 elements (e.g., the blocks  $OFEB$  and  $OFDE$ ) and those that already ex-  
 334 isted (e.g., the block  $ODBH$ ). Moreover, subdividing these adjacent blocks  
 335 ensures that the newly formed discontinuities are connected (e.g., the dis-  
 336 continuities  $OFE$  and  $OEH$ ), thus enabling immediate benefits from the  $r$   
 337 adaptivity. Due to the fact that only tetrahedral elements are considered,  
 338 some secondary discontinuities (e.g., the discontinuities  $OAG$  and  $OFB$  in  
 339 Fig. 3(a)) are added during the subdivision process. Extending the proposed  
 340 approach to other element shapes would eliminate this requirement.

341 When the local velocity field features the characteristics shown in Fig. 3(b),  
 342 the newly added discontinuities radiate from the axis  $AB$  and bisect the edges  
 343  $OC$  and  $OD$ , and there are many possible ways to distinguish the above two  
 344 different flow directions. The one employed in this work is given by

$$\begin{cases} \text{rotate about } AB & \text{if } \Delta v_i r_i < 0 \\ \text{rotate about } O & \text{if } \Delta v_i r_i \geq 0 \end{cases} \quad (13)$$

345 where  $\Delta v_i = v_i^I - v_i^{II}$ , with  $v_i^I$  and  $v_i^{II}$  denoting the element velocities pointing  
 346 toward and away from the shared surface  $OAB$  shown in Fig. 3, respectively.  
 347 The variable  $r_i$  in Eq. (13) represents a unit vector pointing from  $O$  to  $M$ . It  
 348 is used as a reference direction for distinguishing the direction of the velocity  
 349 jump. When a pair of elements have velocities that both point toward or  
 350 away from the interface ( $OAB$  in Fig. 3), they will not be divided in the  
 351 current iteration, due to the ambiguity of the flow direction.

352     Figure 3 shows only one of three possible permutations, namely the flow  
 353   direction of the local velocity field can also rotate about the other two pairs:  
 354   (1) the point  $A$  paired with the axis  $BO$  and (2) the point  $B$  paired with  
 355   the axis  $AO$ . These three possibilities are distinguished by projecting the  
 356   velocity jump to the three edges of the triangle  $OAB$ . The edge with the  
 357   least projection is the one to which the velocity jump has the greatest per-  
 358   pendicular component, and thereby the one about which the local velocity  
 359   flow tends to rotate. Mathematically, this criterion can be expressed as

$$\begin{cases} \text{rotate about } O/AB & \text{if } |\Delta v_i o_i| \leq \min(|\Delta v_i p_i|, |\Delta v_i q_i|) \\ \text{rotate about } A/BO & \text{if } |\Delta v_i p_i| \leq \min(|\Delta v_i o_i|, |\Delta v_i q_i|) \\ \text{rotate about } B/AO & \text{if } |\Delta v_i q_i| \leq \min(|\Delta v_i o_i|, |\Delta v_i p_i|) \end{cases} \quad (14)$$

360   where  $o_i$ ,  $p_i$  and  $q_i$  denote vectors along edges  $AB$ ,  $BO$  and  $AO$ , respectively.

361   Elements adjacent to stationary regions are subdivided as illustrated in  
 362   Fig. 4. Specifically, the element is divided by creating a new discontinuity  
 363   that radiates from the point  $O$  and bisects the edges  $AC$  and  $BC$ . The

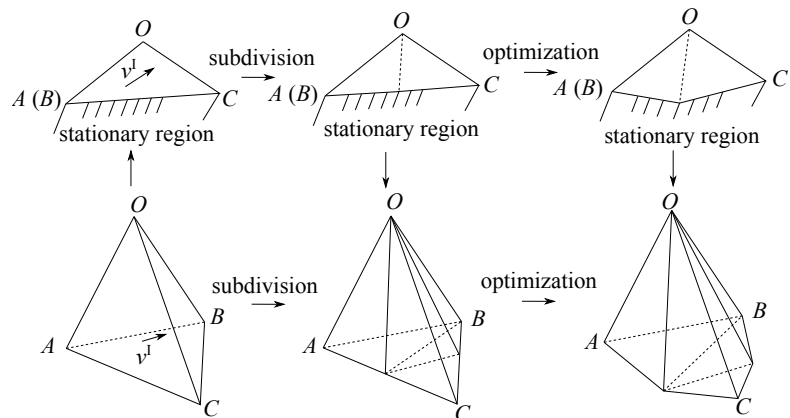


Figure 4: Schematic showing subdivision of a moving block adjacent to stationary region.

364 decision as to which edges to bisect are determined in a manner similar to  
365 Eq. (14). In the rightmost figures, we show the new nodes in their optimized  
366 positions (off of plane  $ABC$ ) to illustrate that this type of subdivision enables  
367 an accurate resolution of the boundary between moving material and the  
368 stationary region, which is typically a discontinuity whose shape is not known  
369 beforehand.

## 370 6. Algorithm summary

371 The complete algorithm for the proposed  $r$ - $h$  adaptive method is summa-  
372 rized in the main flow chart of Fig. 2. The computations start by optimizing  
373 the nodal positions of the initial mesh. Then, the algorithm repeats the cycle  
374 of subdividing elements and adjusting nodal positions, until satisfying either  
375 of the following two criteria: (1) the relative improvement of the limit load  
376 between two consecutive subdivisions is less than a prescribed tolerance, de-  
377 noted by  $F_{tol}$ , or (2) no element needs to be subdivided. It should be noted  
378 that, in the above-mentioned cycle, any  $h$  adaptivity step is immediately fol-  
379 lowed by an  $r$  adaptivity step. The reason why we do not allow consecutive  
380  $h$  adaptivity steps will be elaborated by the numerical examples detailed in  
381 Section 7.

382 As in any numerical approach, the question arises as to how to select the  
383 various tolerances introduced above. For the numerical examples discussed  
384 later, trial and error revealed that the following choices of tolerances give  
385 satisfactory performance:  $F_{tol} = 0.1$ ,  $\Delta v_{tol} = v_0$ ,  $v_{tol} = 0.01v_0$ , where  $v_0$  de-  
386 notes the magnitude of the velocity along the boundary where the limit load  
387 is evaluated. Because the volume filtering mechanism described above can

388 potentially stop subdivision prematurely, a small value of  $1E^{-3}b^3$  is assigned  
389 to the tolerance  $V_{tol}$ , where  $b$  is the largest dimension of the loading area.

390 **7. Example problems**

391 To explore the performance of the proposed method, three examples are  
392 studied: (1) bearing capacity of a square foundation on cohesionless soil or  
393 purely cohesive soil; (2) passive uplift resistance of a square, horizontal anchor  
394 embedded in cohesionless soil; and (3) passive resistance of a rectangular  
395 retaining wall in cohesionless soil.

396 *7.1. Bearing capacity of a square foundation*

397 The limit load for a square surface foundation of width  $b$  on cohesionless  
398 soil can be expressed as

$$F = \frac{1}{2}\gamma b^3 N_{\gamma s} \quad (15)$$

399 In Eq. (15), the dimensionless quantity  $N_{\gamma s}$  is a function of the internal friction  
400 angle  $\phi$  and the interfacial roughness between the footing and the soil.  
401 The subscript “s” is used to distinguish this factor, for a square foundation,  
402 from the 2D (plane strain) bearing capacity factor commonly denoted as  
403  $N_\gamma$ . Exact values for  $N_\gamma$  were obtained numerically by Martin (2005), who  
404 performed detailed calculations based on the method of characteristics and  
405 utilized, notably, adaptive subdivision in his approach. In 3D, exact theoretical  
406 solutions remain elusive, and  $N_{\gamma s}$  in particular is an unknown function.  
407 However, upper bounds obtained through limit analysis have been evaluated  
408 semi-analytically and numerically (Michałowski, 2001; Krabbenhøft et al.,  
409 2008; Lyamin et al., 2007). This work models cohesionless soils by assigning

410 zero-valued cohesion  $c$  to the dissipated power (Eq. 10). The unit weight of  
 411 the soil  $\gamma$  and the footing width  $b$  are each assumed to be 1 for ease in inter-  
 412 preting  $N_{\gamma s}$ . The relative slip between the footing and the soil is prevented  
 413 (i.e., perfectly rough) in the simulation.

414 To initiate the computation, one has to guess an initial mesh. For refer-  
 415 ence, we consider the mechanism constructed by Michalowski (2001) rendered  
 416 in Fig. 5(a). This mechanism is characterized by a single pyramidal block  
 417 that moves downward vertically with the foundation and four adjacent re-  
 418 gions composed of rigid blocks truncated by conical surfaces. For clarity, Fig.  
 419 5 shows only one of the four regions. By comparison, the starting guess con-  
 420 sidered in this work is extremely simple. It is depicted in Fig. 5(b). Taking  
 421 advantage of the four-fold symmetry (i.e.,  $OMN$  shown in Fig. 5(a) represents  
 422 a  $45^\circ$  slice of the footing), the mesh consists of only three elements (blocks),  
 423 one directly beneath the foundation and two that are adjacent. Initially, one

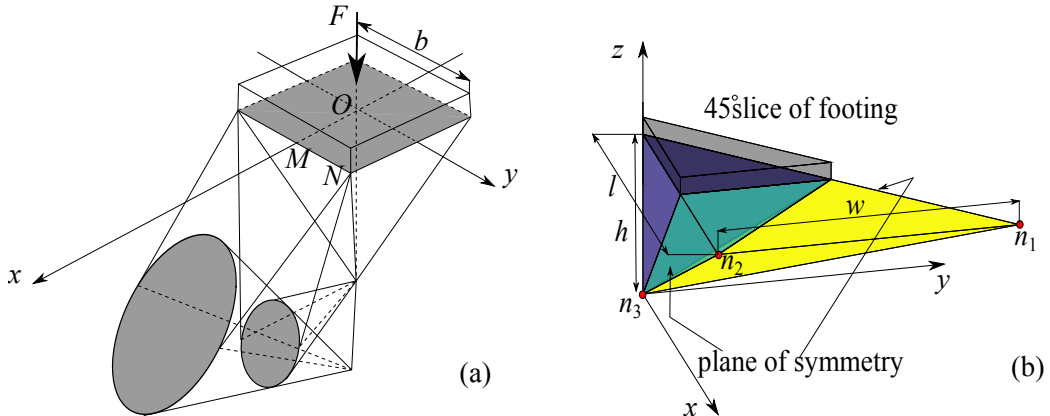


Figure 5: Bearing capacity of a rough rigid square foundation on cohesionless soils: (a) multi-block mechanism (adapted from Michalowski (2001)); (b) initial mesh assumed in the  $r$ - $h$  adaptive approach.

424 has to guess the positions of the nodes  $n_1$ ,  $n_2$ , and  $n_3$  (or equivalently the  
 425 values of three geometric variables  $h$ ,  $l$  and  $w$  in Fig. 5(b)). Throughout the  
 426  $r$ - $h$  adaptive optimization procedure (Fig. 2), these nodes are constrained  
 427 to move parallel to the plane of symmetry in which they reside,  $y = 0$  or  
 428  $x = y$ , as are any nodes within these planes added through adaptive sub-  
 429 division. Additionally, the components of velocity normal to the planes are  
 430 constrained to be zero.

431 When the friction angle is high, the jump condition given by Eq. (2)  
 432 becomes increasingly restrictive with respect to finding a kinematically ad-  
 433 missible velocity field for a particular mesh. Consequently, the existence of  
 434 a feasible solution for SOCP becomes sensitive to the mesh geometry, and  
 435 selecting initial values for the above geometric variables becomes challeng-  
 436 ing. This issue was resolved by sequentially optimizing the nodal positions  
 437 while gradually increasing the friction angle. In other words, one can start  
 438 the computation by (1) introducing a low, fictitious friction angle denoted  
 439 by  $\phi_0$ , (2) optimizing the nodal positions, and (3) using the optimized mesh  
 440 as a starting guess to obtain a feasible initial solution for a higher friction  
 441 angle. The procedure is repeated until the true friction angle is reached. In  
 442 this work, the starting guess in all cases was  $h = b/2$ ,  $w = b$ , and  $l = b$  with  
 443  $\phi_0 = 10^\circ$ .

444 The solid line in Fig. 6 shows the computed values of  $N_{\gamma s}$  for  $\phi = 35^\circ$   
 445 as they vary for each iteration of the SQP algorithm utilized within the  
 446 proposed  $r$ - $h$  adaptive solution procedure to solve Eq. (12). The figure shows  
 447 that the computed upper bound on  $N_{\gamma s}$  rapidly decreases as the iteration  
 448 number increases, highlighting the sensitivity of the solution to the mesh,

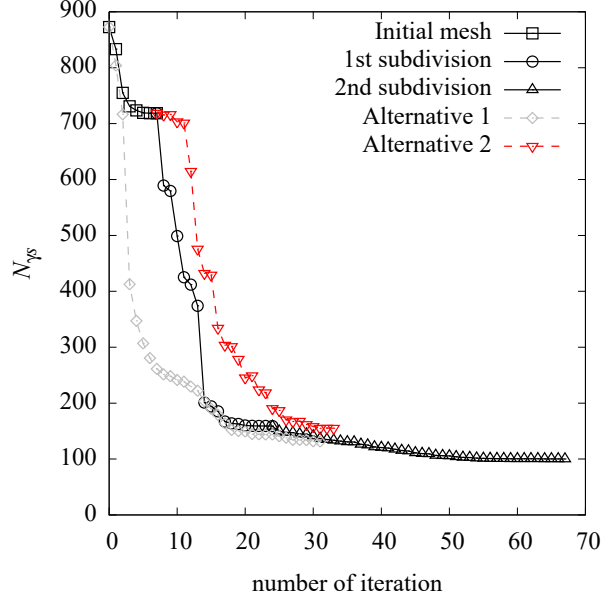


Figure 6: Variation of the  $N_{\gamma_s}$  value as a function of the iteration numbers in the non-linear optimization ( $\phi = 35^\circ$ ).

and thus also revealing the effectiveness of  $r$  adaptivity. In this example, the method resulted in two subdivisions. The initial mesh and the meshes corresponding to these subdivisions are presented in Figs. 7(a)-(c), wherein the number of elements after each subdivision is also provided. Prior to each subdivision, the convergence curve becomes flat, signaling that better upper bounds cannot be reached for the current mesh. Through the use of  $h$  adaptivity, the computed limit load can be further reduced, and a faster convergence rate can be recovered (e.g., 1st subdivision in Fig. 6). The reason why  $h$  adaptivity is effective is revealed in Fig. 7. Comparing the initial mesh to those obtained after subdivision, the approach enables the creation of more velocity discontinuities radiating outward from the edge

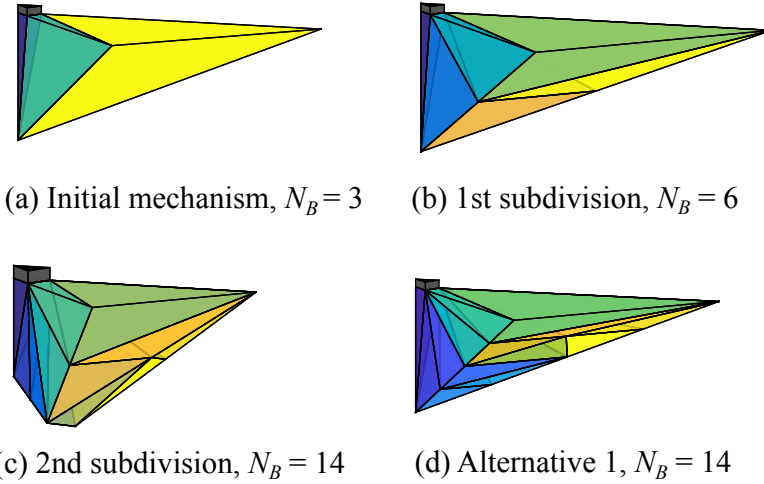


Figure 7: Mesh before and after element subdivisions ( $\phi = 35^\circ$ ).

460 of the footing. Moreover, the lowermost part of the collapse mechanism is  
 461 gradually divided in a way that the above radial discontinuities can extend all  
 462 the way to the boundary of the region of failing (moving) soil. Both features  
 463 are important in forming a radial shearing zone, which accommodates the  
 464 rotation of the principal directions of strain.

465 Figure 6 highlights the fact that the rate of improvement in the solution  
 466 generally diminishes as the  $r$ - $h$  adaptive iterations proceed. This response  
 467 may be attributed to two possible explanations. The first hypothesis is that  
 468 the smaller element sizes obtained through  $h$  adaptivity constrain the mag-  
 469 nitude of nodal position changes that can occur in the optimization, due  
 470 to the imposed non-linear constraints requiring no interpenetration between  
 471 elements (see Eq. (12)). This reduces the amount that nodes are able to  
 472 perturb around their current positions, thereby demanding more  $r$ -adaptive  
 473 iterations to achieve a better mechanism. The second hypothesis is that, as  
 474 the current mechanism is closer to the optimum, the optimization algorithm

475 adopts smaller step size (i.e., nodal perturbation during one iteration), and  
476 consequently the rate of improvement is reduced.

477 To test these two hypotheses, we consider an alternative initial mesh with  
478 the same overall geometry as the original one (Fig. 7(a)) but with the same  
479 connectivity and number of elements as in the final solution (Fig. 7(c)). Com-  
480 pared with the original starting guess, this new initial mechanism (Fig. 7(d))  
481 simply has smaller initial element sizes. The dashed line in Fig. 6 designated  
482 by “Alternative 1” shows that the  $r$  adaptive iterations are more effective  
483 for the new initial mesh with smaller element sizes. This reveals that the  
484 deterioration in the effectiveness of  $r$  adaptivity is not related to the number  
485 and size of elements but rather due to the fact that an optimal mechanism is  
486 approached (the second of the two hypotheses above). One might infer from  
487 the above discussion that starting from a more refined mesh is generally  
488 more effective, given that better results are achieved with fewer iterations.  
489 However, this is not the case, since the refined solution with element edges  
490 (velocity discontinuities) placed at strategic locations is known only after  
491 refinements are obtained through iterations of  $r$ - $h$  adaptivity.

492 We use the data corresponding to “Alternative 2” in Fig. 6 to illustrate  
493 why an  $r$  adaptive step is employed immediately following any  $h$  adaptive  
494 step, as described in Section 6. In Alternative 2, two consecutive  $h$  adaptive  
495 steps are performed on the initial mesh depicted in Fig. 7(a). The nodal  
496 positions of this refined mesh are then optimized using  $r$  adaptivity. Fig-  
497 ure 6 shows that after multiple  $h$  adaptive steps,  $r$  adaptivity becomes less  
498 efficient compared with the proposed algorithm. This can be explained as  
499 follows. When only subdividing elements without optimizing nodal positions,

500 the elements on both sides of the new discontinuities have the same velocity  
 501 as if the original elements have yet to be subdivided, and there are no  
 502 velocity jumps across these new discontinuities. These new discontinuities  
 503 with zero velocity jumps do not provide effective information regarding how  
 504 to refine the mesh (see Section 5). This analysis shows that simply increasing  
 505 the number of elements often does not lead to an improved solution. It  
 506 underscores the merit of the proposed approach, which starts from a simple  
 507 mesh that is progressively refined through combined  $r$ - $h$  adaptivity.

508 Figure 8 presents the  $N_{\gamma s}$  values computed with the proposed method for  
 509 friction angles from  $\phi = 15^\circ$  to  $35^\circ$ . For the purpose of comparison, the exist-  
 510 ing semi-analytical solution of Michalowski (2001) and the FELA results of

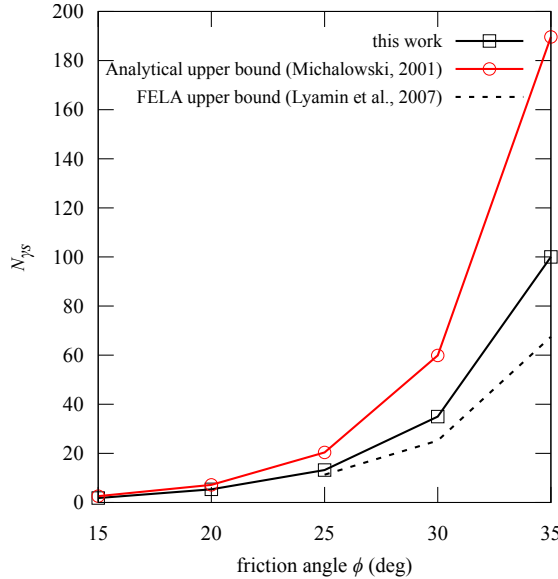


Figure 8: Comparison of  $N_{\gamma s}$  values computed from the proposed method and existing solutions.

511 Lyamin *et al.* (2007) are included in the figure. Figure 8 shows that the pro-  
 512 posed method gives a better (smaller) solution than the analytical approach,  
 513 with the improvement increasing as the friction angle grows. On the other  
 514 hand, the  $N_{\gamma s}$  values computed in the present study are larger than the ones  
 515 given by FELA, with the difference again tending to increase as the friction  
 516 angle increases. Such a discrepancy between these two methods might be at-  
 517 tributed to the continuous deformation allowed within elements in FELA.  
 518 Through the use of rigid elements, the implementation presented in this work  
 519 is potentially restrictive in the manner in which it accommodates the dilation  
 520 of soils with large friction angles. Nevertheless, the ability of such a simple  
 521 approach, and relatively simple collapse mechanism, to capture reasonable  
 522 values of the limit load for such a challenging problem is remarkable.

523 Figure 9 compares the computed failure mechanisms for different friction

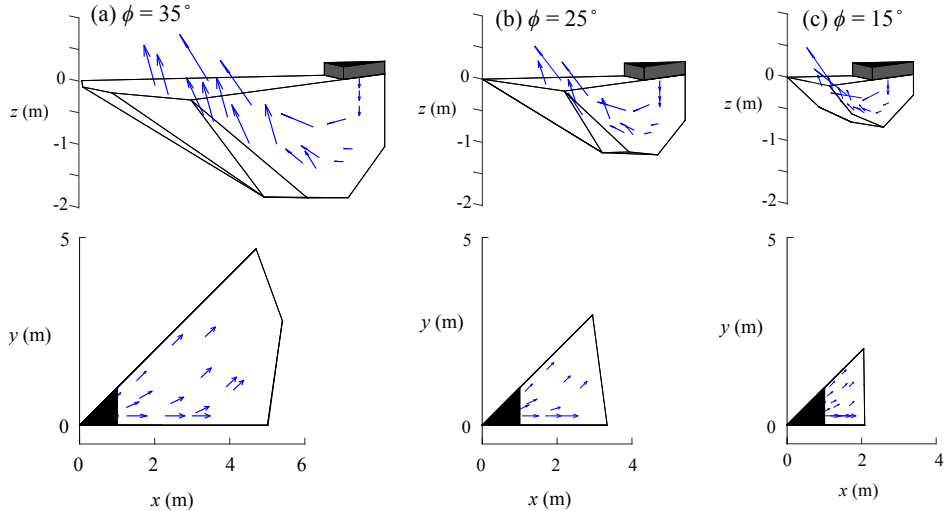


Figure 9: Optimal failure mechanism beneath the square foundation computed with the proposed approach: (a)  $\phi = 35^\circ$ ; (b)  $\phi = 25^\circ$ ; (c)  $\phi = 15^\circ$ .

524 angles. As a matter of clarity, some block edges are removed from the figure.  
525 It should be emphasized that while all three mechanisms start from the  
526 same guess in terms of the initial mesh (Fig. 5(b)), they automatically evolve  
527 depending on the friction angle of the material. For larger friction angles, the  
528 failure mechanism extends both horizontally and vertically a larger distance  
529 compared to solutions with lower friction angles.

530 To further test the proposed method, especially against existing tech-  
531 niques, the problem of a square foundation on cohesive soil is analyzed. The  
532 limit load for this problem, first considered by Shield and Drucker (1953),  
533 can be expressed in terms of the soil cohesion  $c$  as

$$F = cb^2 N_{cs} \quad (16)$$

534 where  $N_{cs}$  is a constant. Computations were completed in the same manner  
535 as for  $N_{\gamma s}$ , using the same initial guess for the mesh as described above  
536 (Fig. 5(b);  $h = b/2$ ,  $w = b$ , and  $l = b$ ). The unit weight of soils is assumed  
537 to be zero and the cohesion  $c$  is equal to 1.

538 Table 1 compares the  $N_{cs}$  values computed in this study to those ob-  
539 tained semi-analytically (Michalowski, 2001), using FELA (Vicente da Silva  
540 and Antão, 2008), and using DLO (Hawksbee et al., 2013). The recorded  
541 or reported computation time for each numerical method is also included.  
542 Calculations in this study were completed on a PC equipped with an Intel  
543 i7-4790 processor (3.6 GHz; 4 cores) and 8 GB memory. Results from FELA  
544 were obtained by distributing computations over 5 or 18 PCs, where each  
545 PC was equipped with a single core processor clocked at 3.0 GHz (Intel Pen-  
546 tium IV) and 512 MB memory. The DLO computations were performed on  
547 a workstation equipped with an AMD Opteron 6140 processor (2.6 GHz; 8

Table 1: Comparison of computed  $N_{cs}$  values by different methods with corresponding computation costs (wall-clock time: the total processing time, including time spent on pre-processing, kernel computation through the FMINCON function and MOSEK, and post-processing; MOSEK time: the processing time spent on solving the second-order cone programming through MOSEK).

Analytical		FELA		DLO		This work			
upper	upper	upper	upper	node spacing	$N_{cs}$	MOSEK times	subdivision	$N_{cs}$	wall-clock times
bound	bound					(s)			(s)
6.56	6.05	2000	1/2	6.52	0.02	0	8.27	0.96	0.2
			to		1/4		1	6.67	2.0
			15000		1/6	6.22	2	6.44	4.4

cores) and 8 GB memory, and only the CPU times for SOCP with Mosek were reported. Because the basic computation unit in the proposed  $r$ - $h$  adaptive approach is solving Eq. (10) using SOCP, the CPU times for executing Mosek are separated from the total wall-clock times. Due to differences in the hardware and the particulars of programming (e.g., language and code optimization), the computation times reported in Table 1 are merely indicators of the computation cost rather than strictly comparable performance measures.

Table 1 shows that DLO and the  $r$ - $h$  adaptive approach provide reasonably accurate estimates of the limit load (better than the analytical solution), and that FELA gives the least upper bound (best estimate of the limit load).

559 Compared to DLO and FELA, for which accuracy and computation time de-  
 560 pend strongly on the element size or grid spacing, the  $r$ - $h$  adaptive approach  
 561 displays a significant improvement in the computed limit load without an  
 562 exorbitant increase in computational cost. This difference can be attributed  
 563 to the fact that uniform mesh or grid refinement tends to add a large num-  
 564 ber of additional unknowns that do not contribute towards improving the  
 565 solution. Finally, we note that the CPU times for running Mosek in this  
 566 work are only a small portion of the total times, thus suggesting that the  
 567 reported computational times can be potentially reduced by utilizing more  
 568 efficient optimization schemes and programming languages for the non-linear  
 569 optimization problem posed by  $r$  adaptivity (Section 4).

570 *7.2. Uplift resistance of a plate anchor in cohesionless soil*

571 With reference to the collapse mechanism considered by Murray and Ged-  
 572 des (1987), Fig. 10(a) illustrates the problem of a horizontal anchor problem  
 573 embedded at depth  $h$ . The anchor is square with sides of length,  $b$ , and the  
 574 material is assumed to be cohesionless. The status of “immediate breakaway”  
 575 is considered, which implies that the underside of the anchor loses contact  
 576 with the soil. The ultimate uplift force  $F$  is expressed as

$$F = \gamma b^2 N_{\gamma b} \quad (17)$$

577 The factor  $N_{\gamma b}$  is referred to as the anchor break-out factor, and its value  
 578 depends on  $\phi$ , the ratio of the embedment depth to the anchor width ( $h/b$ ),  
 579 and friction at the soil-anchor interface. For a fixed friction angle of  $\phi = 30^\circ$ ,  
 580 this example considers the  $N_{\gamma b}$  factors corresponding to varying values of  
 581  $h/b$ . Here, as in the previous example, we assume zero-valued cohesion to

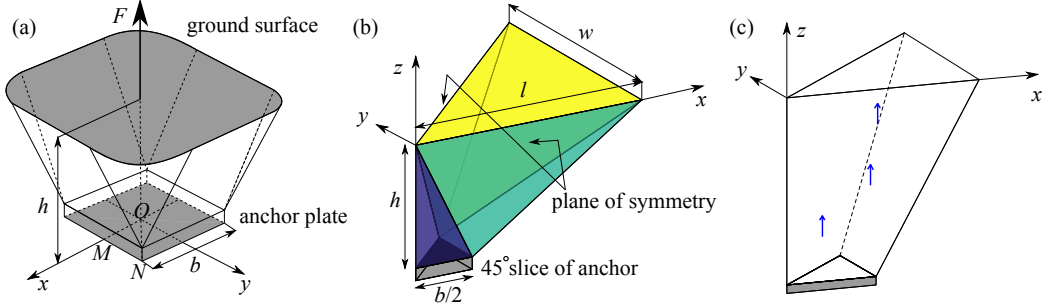


Figure 10: Uplift of an anchor in cohesionless soil: (a) collapse mechanism considered by Murray and Geddes (1987); (b) initial mesh used in the  $r$ - $h$  adaptive approach; (c) typical collapse mechanism computed with the  $r$ - $h$  adaptive approach.

582 model cohesionless soils. The unit weight of the soil  $\gamma$  and the anchor width  
 583  $b$  are each assumed to be 1. Above the anchor, a perfectly rough interface  
 584 is simulated by eliminating relative movement between the anchor and the  
 585 soil.

586 Fig. 10(b) depicts the initial mesh selected for the  $r$ - $h$  adaptive approach.  
 587 As in the previous example, symmetry is invoked to reduce the model to a  
 588 45° slice of the anchor (i.e., slice  $OMN$  in Fig. 10(a)), where the planes  $y = 0$   
 589 and  $x = y$  represent the planes of symmetry. The initial mesh is again one  
 590 of the simplest conceivable, and it consists of three elements. The geometric  
 591 variables  $l$  and  $w$  are initially assumed to be  $2h$ , which leads to feasible initial  
 592 solutions for all embedment ratios.

593 Figure 11 compares the  $N_{\gamma b}$  values computed with the  $r$ - $h$  adaptive ap-  
 594 proach to values obtained in previous works: those obtained with the ana-  
 595 lytical solution of Murray and Geddes (1987) and the 3D DLO analysis of  
 596 Hawksbee et al. (2013). Satisfactory agreement between the three methods  
 597 can be observed for both shallow and deep embedment. Figure 10(c) presents

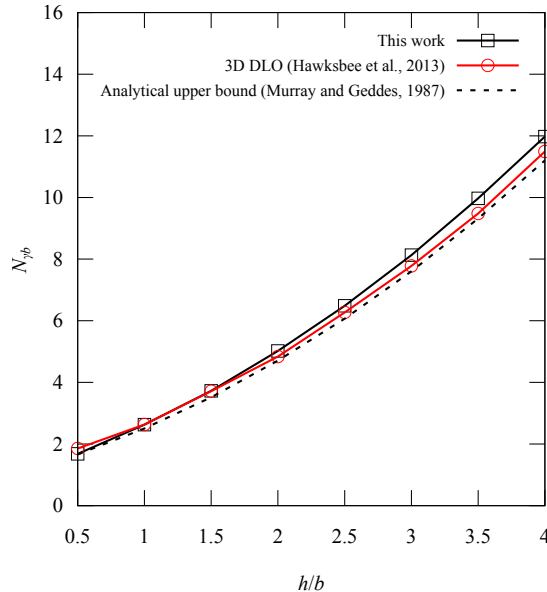


Figure 11:  $N_{\gamma b}$  values computed with the  $r$ - $h$  adaptive approach compared to existing solutions.

598 a typical collapse mechanism computed by this work. The mechanism is char-  
 599 acterized by single active velocity discontinuity that extends from the edge of  
 600 the anchor to the ground surface and bounds a plug of material that moves  
 601 upward with the anchor. This mechanism is similar to the one constructed  
 602 by Murray and Geddes (1987) (Fig. 10(a)), but it differs with respect to the  
 603 the conical surfaces assumed at the edges of the collapse mechanism. With  
 604 these cone-shaped edges, the soil volume lifted by the anchor is reduced, and  
 605 consequently a slightly lower (better) upper-bound solution is obtained, as  
 606 shown in Fig. 11.

607 One possible cause for the above mismatch is that no subdivision step is  
 608 performed for this anchor problem, as all velocity jumps are below the toler-

609 ance for triggering  $h$  adaptivity (i.e.,  $\Delta v_{tol} \leq v_0$ , where  $v_0$  in this example is  
 610 the anchor velocity). Accordingly, we lowered the tolerance  $\Delta v_{tol}$  to  $0.1v_0$  to  
 611 explore whether the Murray and Geddes (1987)'s solution can be recovered  
 612 by refining the mesh. Figure 12 compares the optimized collapse mechanism  
 613 based on the initial mesh and the refined one. It can be seen that because  
 614 the initial mesh produces a uniform velocity field across elements (i.e., ve-  
 615 locity jumps between elements are zero), only the blocks at the boundary  
 616 of the failing soil volume are subdivided. In other words, this subdivision  
 617 is based exclusively on the velocity jumps between moving blocks (i.e, the  
 618 blocks  $OBDA$  and  $OCDB$  in Fig. 12(a)) and the assumed stationary region.  
 619 Whereas a discontinuity passing the nodes  $D$  and  $O$  and insects the edge  $AB$   
 620 could lead to an improved mechanism, Figure 12(b) shows that the proposed  
 621 subdivision strategy adds new discontinuities that intersect with the failure  
 622 plane  $ABCD$  and do not help in forming a more critical mechanism. As a  
 623 consequence, the elements and discontinuities introduced in the refined mesh

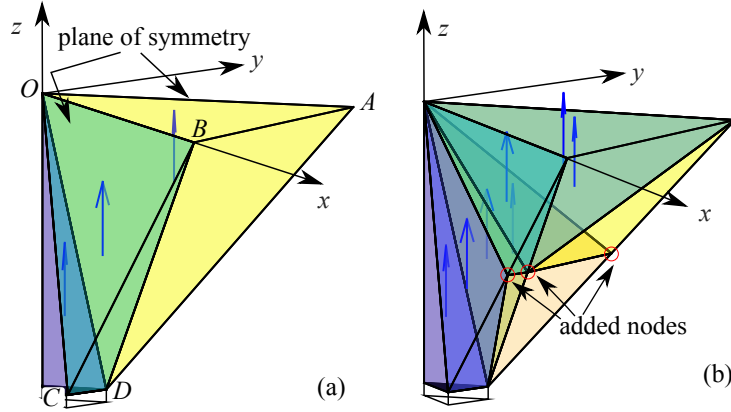


Figure 12: Collapse mechanism after optimizing nodal positions: (a) initial mesh; (b) after first subdivision.

624 do not alter the optimized collapse mechanism or the computed limit load.

625 *7.3. Rectangular wall in cohesionless soil*

626 As a final example, the  $r$ - $h$  adaptive approach is applied to compute the  
 627 limit load on a rectangular retaining wall in cohesionless soil. The problem is  
 628 illustrated in Fig. 13(a), which also depicts the collapse mechanism assumed  
 629 by Soubra and Regenass (2000). The width and height of the wall are denoted  
 630 by  $b$  and  $h$ , respectively, and the wall is assumed to move laterally into the  
 631 soil (passive condition). The passive force on the wall at collapse can be  
 632 expressed as

$$F = \frac{1}{2}\gamma b h^2 K_{\gamma p} \quad (18)$$

633 where  $K_{\gamma p}$  is the so-called passive earth pressure coefficient. Generally, the  
 634 passive resistance depends on the mode of wall movement, and in particu-  
 635 lar whether it translates, rotates, or moves with combined translation and  
 636 rotation (Widuliński et al., 2011). Here, only translational movement is con-  
 637 sidered.

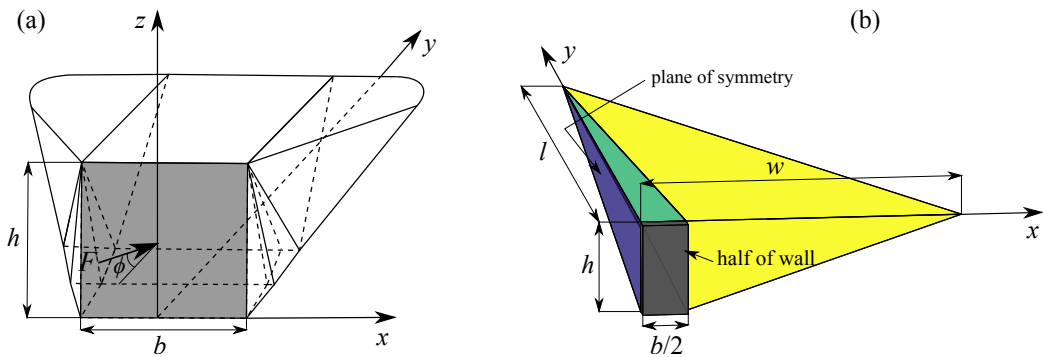


Figure 13: Collapse mechanism for passive failure of a rectangular retaining wall in cohesionless soil: (a) truncated multi-block mechanism (adapted from Soubra and Regenass (2000)); (b) initial mesh assumed in the  $r$ - $h$  adaptive approach.

638 This example models cohesionless soils in the same manner as those dis-  
639 cussed earlier. The unit weight  $\gamma$  is assumed to be 1, and both the wall width  
640  $b$  and height  $h$  are assumed to be 2. Unlike the previous two examples, the  
641 perfectly rough interface between soils and the retaining wall is modeled as  
642 a velocity discontinuity, whose jump condition is characterized by friction  
643 angle  $\phi$ . This change is made in accordance with the assumption in the work  
644 of Soubra and Regenass (2000), thus enabling a direct comparison.

645 Figure 13(b) shows the starting mesh used to initiate the computation.  
646 Considering that  $x = 0$  is a plane of symmetry, only half of the wall is  
647 modeled. The geometric variables  $l$  and  $w$  are initially assumed to be  $2h$ ,  
648 and are adjusted to  $l = 3.53h$  and  $w = 7.20h$ , for all values of  $\phi$ , by the  
649 sequential optimization discussed in Section 7.1. In this case the direction of  
650 the force  $F$  is not horizontal but inclined at an angle  $\phi$  with respect to the  
651 direction normal to the wall (see Fig. 13(a)).

652 Figure 14 compares the  $K_{\gamma p}$  values computed in this study and to those  
653 assessed using the analytical solution proposed by Soubra and Regenass  
654 (2000). The analytical solution corresponds to the failure mechanism shown  
655 in Fig. 13(a), which consists of multiple blocks truncated by portions of cir-  
656 cular cones. The methods provide very close results for small friction angles.  
657 As the friction angle increases, the  $r$ - $h$  adaptive approach gives lower (better)  
658 estimates of the limit load.

659 The collapse mechanisms assessed through the  $r$ - $h$  adaptive approach for  
660 large and small friction angles are presented in Fig. 15. While both cases start  
661 from the same initial mechanism, the proposed adaptive approach allows for  
662 the mechanism to extend to greater depth and horizontal distance as the

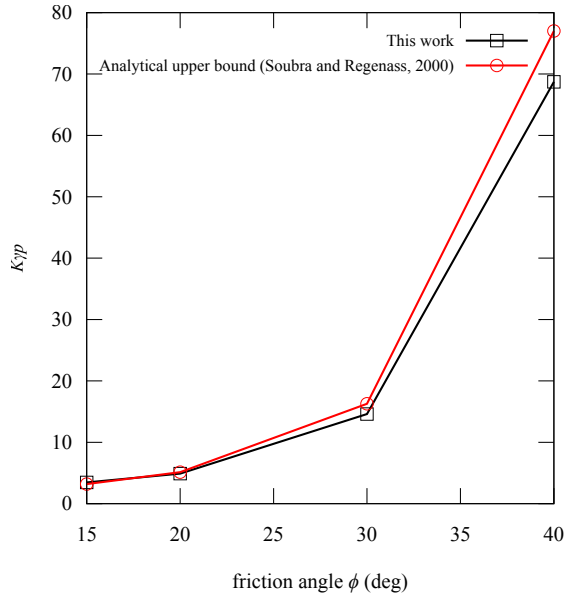


Figure 14: Comparison of the passive earth pressure coefficients  $K_{\gamma p}$  computed by this work and the analytical solution of Soubra and Regenass (2000).

663 friction angle grows, as in the solution of Soubra and Regenass (2000).

664 **8. Discussion**

665 Table 2 summarizes the computational cost of the  $r$ - $h$  adaptive approach  
 666 for the three examples considered. The table includes the number of rigid  
 667 blocks ( $N_B$ ), the number of nodal position components subjected to op-  
 668 timization ( $DOF$ ), wall-clock times, and the CPU times required to run  
 669 MOSEK. Such information is organized for both the initial mesh configura-  
 670 tion and those after  $h$  adaptivity steps. For these examples, the  $r$ - $h$  adaptive  
 671 approach displays promising computational efficiency. The maximum com-  
 672 putation time is no more than 30 seconds, observed in the square footing

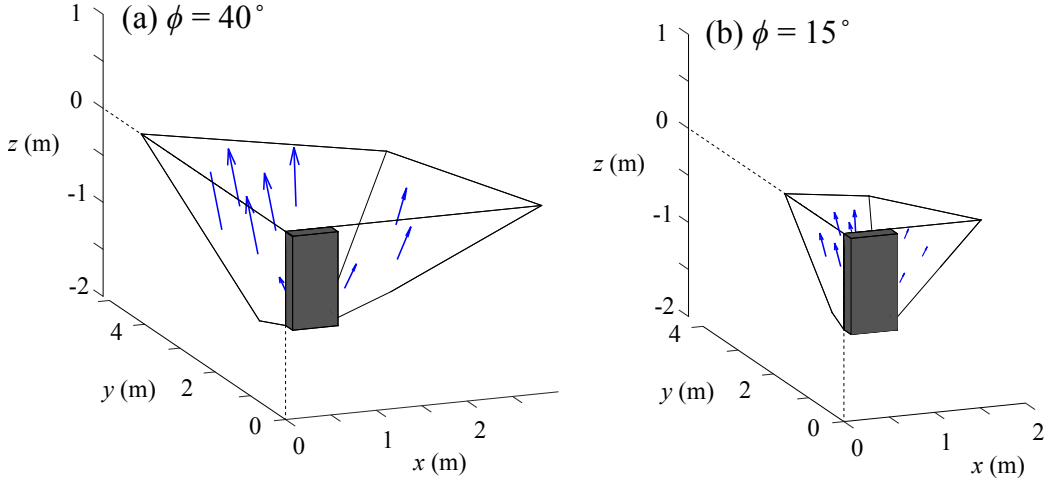


Figure 15: Collapse mechanisms computed with the  $r$ - $h$  adaptive approach: (a)  $\phi = 40^\circ$ ; (b)  $\phi = 15^\circ$ .

Table 2: Computational cost for the three examples.

Example	subdivision	$N_B$	$N_{DOF}$	wall-clock time (s)	MOSEK time (s)
square footing	0	3	3	0.8 to 1.2	0.1 to 0.3
	1	5 to 6	5 to 7	2.0 to 4.3	0.4 to 0.6
	2	11 to 14	11 to 18	4.4 to 21.2	0.9 to 4.2
retaining wall	0	3	2	1.7 to 2.1	0.6 to 0.7
	1	10 to 11	10 to 14	1.8 to 9.4	0.4 to 1.6
square anchor	0	3	2	1.8 to 2.2	0.7 to 0.8

673 case. The fact that the maximum MOSEK running time is around 4 seconds  
 674 suggests that the approach could also be accelerated by formulating a more  
 675 efficient strategy to solve the non-linear optimization problem of Eq. (12),  
 676 rather than using the FMINCON solver available in MATLAB.

677 While the above computation times are promising, they are not yet suf-

678 ficiently small to enable highly efficient sequential kinematic analysis for 3D  
679 applications, one of the underlying objectives of this work. The computa-  
680 tional demands of the proposed approach can be traced to the fact that a  
681 forward numerical differentiation is employed to compute the gradient of the  
682 objective function in the non-linear optimization. In other words, the ob-  
683 jective function (the SOCP problem of Eq. 10) is called *DOF* + 1 times  
684 to obtain the gradient. Therefore, computing the gradient consumes a sig-  
685 nificant amount of time when *DOF*, corresponding to the number of nodal  
686 positions, becomes large. To improve the computational efficiency, a future  
687 refinement of the current work could be to approximate rather than directly  
688 compute the gradient. For instance, the objective function can be linearized  
689 with respect to its unknowns (cf. Hambleton and Sloan, 2013; Milani and  
690 Lourenço, 2009), thus rendering an approximated but analytical form of the  
691 gradient.

692 Compared with previous works on *r* adaptivity, an important contribu-  
693 tion of this work is the adaptive subdivision, which automatically changes the  
694 topological connectivity of blocks based on velocity jumps between blocks.  
695 Table 3 summarizes the computed limit loads under initial mesh configura-  
696 tion and after subsequent subdivisions. It can be seen that the calculated  
697 upper bounds significantly decrease as the mesh is gradually refined, thus  
698 suggesting that element subdivision based on the velocity jump is effective  
699 in improving the collapse mechanism. Table 3 reports the computed results  
700 only up to 2 subdivisions. The reason is that further mesh refinements only  
701 lead to marginal improvement on the collapse loads. For example, additional  
702 mesh refinement only decreases the computed  $N_{\gamma_s}$  value in the square foot-

Table 3: Limit loads computed by the initial mesh and after element subdivision (all reported values are obtained after optimizing nodal positions).

Numerical example	$\phi$ (°)	initial mesh	1st subdivision	2nd subdivision
square footing $N_{\gamma s}$ or $N_{cs}$	35	718.6	159	100.2
	30	150.5	50.9	35.0
	25	41.9	17.9	13.2
	20	13.6	6.6	5.4
	15	4.8	2.4	1.8
	0	8.3	6.7	6.4
retaining wall $K_{\gamma p}$	40	699.7	68.7	-
	30	23.9	14.6	-
	20	5.8	4.9	-
	15	3.5	3.5	-

703 ing example by less than 5%, while the coefficient  $K_{\gamma p}$  in the retaining wall  
 704 problem remains unchanged even more subdivisions are performed.

705 The fact  $r$ - $h$  adaptive approach eventually reaches a limit of no improve-  
 706 ment can be attributed to two reasons. First, as demonstrated explicitly  
 707 in Section 7.2, the proposed subdivision scheme does not always lead to an  
 708 improvement in the solution. Indeed, the development of a more sophisti-  
 709 cated subdivision strategy is an matter for future investigation. Such future  
 710 algorithms can be devised by (1) identifying other useful indicators that flag  
 711 the regions to be refined and (2) devising effective methods to subdivide  
 712 elements so that discontinuities can be added at strategic locations. The  
 713 second reason is that the algorithm used to solve the non-linear optimization  
 714 is only a local optimizer, and the solution is susceptible to being trapped at  
 715 a point that is a local rather than global optimum. The likelihood of this

716 occurring increases as elements are subdivided, since the the number of  
717 unknowns (nodal positions) handled by the optimization is higher. As a part  
718 of future work, global optimization techniques (e.g., genetic algorithm) can  
719 be employed to resolve this potential limitation.

720 The initial mesh used as a starting guess in the proposed algorithm also  
721 plays a significant role in the accuracy of the computed solution and whether  
722 or not a global minimum can be attained. As made evident in the results  
723 shown in Table 1, 3D DLO with a coarse grid may provide a reasonable  
724 estimate of the limit loads at low cost, thus representing an encouraging  
725 approach to systematically define initial meshes that can subsequently be  
726 refined using the approach proposed in this work.

727 **9. Conclusions**

728 We propose an  $r$ - $h$  adaptive kinematic approach for computing collapse  
729 mechanisms and limit loads in 3D problems. Considering a velocity field  
730 consisting of rigid elements (blocks) separated by zero-thickness velocity dis-  
731 continuities, this method progressively improves the collapse mechanism and  
732 bound on the limit load by successively adjusting the element nodal positions  
733 ( $r$  adaptivity) as well as the element number and connectivity ( $h$  adaptivity).  
734 Examination of the proposed technique through examples shows that when  
735 the optimal mechanism is relatively simple, satisfactory limit loads can be  
736 obtained solely by optimizing nodal positions (i.e., the locations of velocity  
737 discontinuities), even if a simple mesh is assumed. However, when the op-  
738 timal collapse mechanism becomes more intricate, adding discontinuities at  
739 critical locations becomes crucial for the performance of  $r$  adaptivity. The

740 subdivision scheme proposed in this work automatically splits existing ele-  
741 ments with velocity jumps greater than a specified threshold, adding new  
742 elements so that velocity jumps can be further reduced through  $r$  adap-  
743 tivity. This approach allows for the initiation of calculations from a very  
744 simple mesh to which new discontinuities are progressively added at critical  
745 locations, a paradigm that gives demonstrably high efficiency and may yield  
746 higher efficiencies with future refinements.

747 To further speed up computations and enable efficient sequential kine-  
748 matic analysis, wherein a full process of deformation is simulated through  
749 a series of kinematic limit analysis computations, the proposed method can  
750 be improved by pursuing alternatives to solving the non-linear optimiza-  
751 tion of Eq. (12), devising more effective subdivision schemes, and developing  
752 a systematic means of defining the initial mesh. These future refinements  
753 represent important steps towards efficiently simulating large deformation  
754 problems, especially those involving cohesionless soils, that are extremely  
755 challenging to model by any other means.

## 756 10. Acknowledgements

757 Aspects of this work were supported by the Australian Research Council  
758 through the award of Discovery Early Career Researcher Award (DE160100328)  
759 and by the National Science Foundation (CMMI-1742849). This support is  
760 gratefully acknowledged.

761 **References**

762 Antão, A. N., Santana, T. G., Vicente da Silva, M., da Costa Guerra, N. M.,  
763 2011. Passive earth-pressure coefficients by upper-bound numerical limit  
764 analysis. Canadian Geotechnical Journal 48 (5), 767–780.

765 Borges, L., Feijó, R., Zouain, N., 1999. A directional error estimator for  
766 adaptive limit analysis. Mechanics Research Communications 26 (5), 555–  
767 563.

768 Borges, L., Zouain, N., Costa, C., Feijó, R., 2001. An adaptive approach  
769 to limit analysis. International Journal of Solids and Structures 38 (10),  
770 1707–1720.

771 Chen, W.-F., 1975. Limit Analysis and Soil Plasticity. Elsevier.

772 Ciria, H., Peraire, J., Bonet, J., 2008. Mesh adaptive computation of upper  
773 and lower bounds in limit analysis. International journal for numerical  
774 methods in engineering 75 (8), 899–944.

775 Davis, E. H., 1968. Theories of plasticity and the failure of soil masses. In:  
776 Lee, I. K. (Ed.), Soil Mechanics: Selected Topics. Butterworths, Sydney,  
777 pp. 341–380.

778 Davis, E. H., Booker, J. R., 1971. The bearing capacity of strip footing  
779 from the standpoint of plasticity theory. In: Proc. the First Australia-New  
780 Zealand Conference on Geomechanics.

781 Drescher, A., 1991. Analytical Methods in Bin-Load Analysis. Vol. 36 of  
782 Developments in Civil Engineering. Elsevier.

783 Drescher, A., Detournay, E., 1993. Limit load in translational failure mech-  
784 anisms for associative and non-associative materials. *Géotechnique* 43 (3),  
785 443–456.

786 Dunne, H. P., Martin, C. M., 2017. Capacity of rectangular mudmat foun-  
787 dations on clay under combined loading. *Géotechnique* 67 (2), 168–180.

788 Godwin, R., O'Dogherty, M., 2007. Integrated soil tillage force prediction  
789 models. *Journal of Terramechanics* 44 (1), 3–14.

790 Griffiths, D. V., Marquez, R. M., 2007. Three-dimensional slope stability  
791 analysis by elasto-plastic finite elements. *Géotechnique* 57 (6), 537–546.

792 Hambleton, J. P., 2017. Earthmoving through the lens of geotechnical engi-  
793 neering. In: 6th International Young Geotechnical Engineers Conference  
794 (iYGEC6), Seoul, Korea, Sept. 17-22.

795 Hambleton, J. P., Drescher, A., 2012. Approximate model for blunt objects  
796 indenting cohesive-frictional materials. *International Journal for Numerical  
797 and Analytical Methods in Geomechanics* 36 (3), 249–271.

798 Hambleton, J. P., Sloan, S. W., 2013. A perturbation method for optimiza-  
799 tion of rigid block mechanisms in the kinematic method of limit analysis.  
800 *Computers and Geotechnics* 48, 260–271.

801 Hambleton, J. P., Sloan, S. W., 2016. A simplified kinematic method for 3D  
802 limit analysis. *Applied Mechanics and Materials* 846, 342–347.

803 Hambleton, J. P., Stanier, S. A., White, D. J., Sloan, S. W., 2014. Modelling

804 ploughing and cutting processes in soils. *Australian Geomechanics* 49 (4),  
805 147–156.

806 Hawksbee, S., Smith, C., Gilbert, M., 2013. Application of discontinuity  
807 layout optimization to three-dimensional plasticity problems. *Proc R Soc  
808 A* 469 (20130009).

809 He, L., Gilbert, M., 2016. Automatic rationalization of yield-line patterns  
810 identified using discontinuity layout optimization. *International Journal of  
811 Solids and Structures* 84, 27–39.

812 Hettiaratchi, D. R. P., Reece, A. R., 1974. The calculation of passive soil  
813 resistance. *Géotechnique* 24, 289–310.

814 Johnson, D., 1995. Yield-line analysis by sequential linear programming. In-  
815 *ternational Journal of Solids and Structures* 32 (10), 1395–1404.

816 Kashizadeh, E., Hambleton, J. P., Stanier, S. A., 2014. A numerical approach  
817 for modelling the ploughing process in sands. In: *Proc. 14th International  
818 Conference of the International Association for Computer Methods and  
819 Advances in Geomechanics*, Kyoto, Japan, Sept. 22-25. pp. 159–164.

820 Kong, D., Martin, C. M., Byrne, B. W., 2017. Sequential limit analysis of  
821 pipe–soil interaction during large-amplitude cyclic lateral displacements.  
822 *Géotechnique* 68 (1), 1–12.

823 Krabbenhoft, K., Karim, M. R., Lyamin, A. V., Sloan, S. W., 2012. Asso-  
824 ciated computational plasticity schemes for nonassociated frictional mate-  
825 rials. *International Journal for Numerical Methods in Engineering* 90 (9),  
826 1089–1117.

827 Krabbenhøft, K., Lyamin, A. V., Sloan, S. W., 2008. Three-dimensional  
828 mohr–coulomb limit analysis using semidefinite programming. Communications  
829 in Numerical Methods in Engineering 24 (11), 1107–1119.

830 Lyamin, A. V., Salgado, R., Sloan, S. W., Prezzi, M., 2007. Two-and three-  
831 dimensional bearing capacity of footings in sand. Géotechnique 57 (8),  
832 647–662.

833 Lyamin, A. V., Sloan, S. W., 2002a. Lower bound limit analysis using non-  
834 linear programming. International Journal for Numerical Methods in En-  
835 gineering 55 (5), 573–611.

836 Lyamin, A. V., Sloan, S. W., 2002b. Upper bound limit analysis using lin-  
837 ear finite elements and non-linear programming. International Journal for  
838 Numerical and Analytical Methods in Geomechanics 26 (2), 181–216.

839 Lyamin, A. V., Sloan, S. W., Krabbenhøft, K., Hjiaj, M., 2005. Lower bound  
840 limit analysis with adaptive remeshing. International Journal for Numeri-  
841 cal Methods in Engineering 63 (14), 1961–1974.

842 Martin, C. M., 2005. Exact bearing capacity calculations using the method  
843 of characteristics. In: Proc. IACMAG. Turin. pp. 441–450.

844 Martin, C. M., 2011. The use of adaptive finite-element limit analysis to  
845 reveal slip-line fields. Géotechnique Letters 1 (4-6), 23–29.

846 Martin, C. M., Makrodimopoulos, A., 2008. Finite-element limit analysis of  
847 mohr–coulomb materials in 3D using semidefinite programming. Journal  
848 of Engineering Mechanics 134 (4), 339–347.

849 Mary, B. C. L., Maillot, B., Leroy, Y. M., 2013. Deterministic chaos in fric-  
850 tional wedges revealed by convergence analysis. International Journal for  
851 Numerical and Analytical Methods in Geomechanics 37 (17), 3036–3051.

852 Michalowski, R., Drescher, A., 2009. Three-dimensional stability of slopes  
853 and excavations. Géotechnique 59 (10), 839–850.

854 Michalowski, R. L., 2001. Upper-bound load estimates on square and rect-  
855 angular footings. Géotechnique 51 (9), 787–798.

856 Milani, G., 2015. Upper bound sequential linear programming mesh adapta-  
857 tion scheme for collapse analysis of masonry vaults. Advances in Engineer-  
858 ing Software 79, 91–110.

859 Milani, G., Lourenço, P. B., 2009. A discontinuous quasi-upper bound limit  
860 analysis approach with sequential linear programming mesh adaptation.  
861 International Journal of Mechanical Sciences 51 (1), 89–104.

862 Mosek, 2015. The mosek optimization toolbox for MATLAB manual. Version  
863 7.1 (Revision 28), 17.

864 Muñoz, J. J., Bonet, J., Huerta, A., Peraire, J., 2009. Upper and lower  
865 bounds in limit analysis: adaptive meshing strategies and discontinu-  
866 ous loading. International Journal for Numerical Methods in Engineering  
867 77 (4), 471–501.

868 Muñoz, J. J., Hambleton, J., Sloan, S. W., 2018. R-adaptivity in limit anal-  
869 ysis. In: Barrera, O., Cocks, A., Ponter, A. (Eds.), Advances in Direct  
870 Methods for Materials and Structures. Springer International Publishing,  
871 Cham, pp. 73–84.

872 Murray, E. J., Geddes, J. D., 1987. Uplift of anchor plates in sand. *Journal*  
873 of Geotechnical Engineering

874 Nocedal, J., Wright, S. J., 2006. Numerical optimization. Springer.

875 Shield, R. T., Drucker, D. C., 1953. The application of limit analysis to  
876 punch-indentation problems. *Journal of Applied Mechanics* 20, 453–460.

877 Sloan, S. W., 1995. Limit analysis in geotechnical engineering. In: Haberfield,  
878 C. M. (Ed.), Proc. Ian Boyd Donald Symposium on Modern Developments  
879 in Geomechanics, Melbourne, Australia, June 7.

880 Sloan, S. W., 2013. Geotechnical stability analysis. *Géotechnique* 63 (7), 531.

881 Smith, C., Gilbert, M., 2007. Application of discontinuity layout optimization  
882 to plane plasticity problems. *Proc R Soc A* 463, 2461–2484.

883 Soubra, A.-H., Regenass, P., 2000. Three-dimensional passive earth pressures  
884 by kinematical approach. *Journal of Geotechnical and Geoenvironmental  
885 Engineering* 126 (11), 969–978.

886 Sturm, J. F., 2002. Implementation of interior point methods for mixed  
887 semidefinite and second order cone optimization problems. *Optimization  
888 Methods and Software* 17 (6), 1105–1154.

889 The MathWorks, Inc, 2018. Optimization Toolbox<sup>TM</sup> User's Guide. The  
890 MathWorks, Inc.

891 Vicente da Silva, M., Antão, A. N., 2008. Upper bound limit analysis with a  
892 parallel mixed finite element formulation. *International Journal of Solids  
893 and Structures* 45 (22), 5788–5804.

894 Widuliński, Ł., Tejchman, J., Kozicki, J., Leśniewska, D., 2011. Discrete  
895 simulations of shear zone patterning in sand in earth pressure problems  
896 of a retaining wall. International Journal of Solids and Structures 48 (7),  
897 1191 – 1209.

898 Wörden, F. T., Achmus, M., 2013. Numerical modeling of three-dimensional  
899 active earth pressure acting on rigid walls. Computers and Geotechnics  
900 51 (Supplement C), 83 – 90.